Journal of Materials Chemistry A

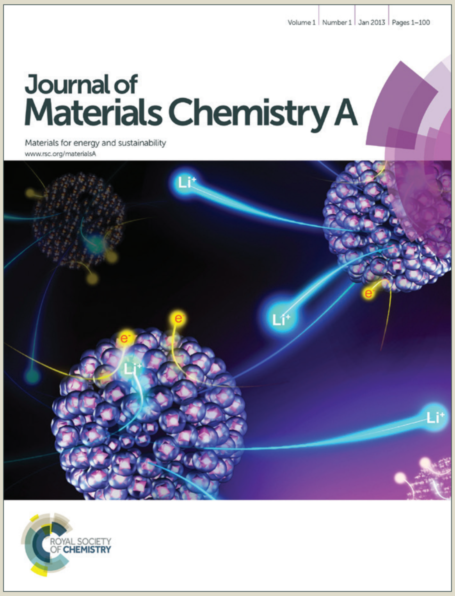

MeO_x/SBA-15 (Me = Zn, Fe): highly efficient nanosorbents for mid-temperature H_2S removal

Mauro Mureddu,[ab] Italo Ferino,[*a] Anna Musinu,[ac] Andrea Ardu,[ac] Elisabetta Rombi,[a]
Maria Giorgia Cutrufello,[a] Paolo Deiana,[d] Marzia Fantauzzi[a] and Carla Cannas[*abc]

[a] *Dipartimento di Scienze Chimiche e Geologiche, Università di Cagliari, s.s. 554 bivio per Sestu, 09042 Monserrato (CA), Italy*
[b] *Consorzio AUSI, Palazzo Bellavista Monteponi, 09016 Iglesias (CI), Italy*
[c] *INSTM, Cagliari Unit*
[d] *ENEA, Centro Ricerche Casaccia, via Anguillarese 301, 00123 S. Maria di Galeria, (Roma), Italy*

*Corresponding authors
Carla Cannas: *ccannas@unica.it*
Italo Ferino: *ferino@unica.it*

Abstract

Zinc oxide/ and iron oxide/SBA-15 composites were synthesized by innovative Two-Solvents procedure and tested as sorbents for the mid-temperature (300 °C) removal of hydrogen sulphide, and compared with a commercial unsupported ZnO sorbent. The sulphur retention capacity results showed the superior performance of the iron oxide/SBA-15 composite (401 mg S/g Fe_2O_3) in comparison with the zinc oxide/SBA-15 one (53 mg S/g ZnO), both these sorbents being much more efficient than the commercial sorbent (6 mg S/g ZnO). The different sorption behaviour was discussed in terms of the nature of the nanocomposites where: (i) the mesostructure of the support is retained, surface area and pore volume being quite high; (ii) the zinc oxide phase is incorporated inside the SBA-15 channels as a thin amorphous homogeneous layer while the iron oxide is dispersed in form of small maghemite crystallites; (iii) significant interactions occur between the silica matrix and the zinc oxide phase. Remarkable differences in the regeneration behaviour of the exhaust sorbents were revealed by temperature-programmed experiments under oxidizing atmosphere. After regeneration the sorption properties of the zinc oxide/SBA-15 composite appeared enhanced compared to the commercial sorbent. Incomplete recovery of the sorption activity was observed for the regenerated iron oxide/SBA-15 sorbent, whose performance remained however far better than that of the ZnO-based one, either fresh or regenerated. In view of its higher sulphur retention capacity and appropriate regeneration temperature (T ≤ 350 °C), the iron oxide/SBA-15 seems a promising material for the design of advanced sorbents for a thermally efficiency H_2S removal process from hot gas streams.

Keywords: Sorbents, Nanocomposites, SBA-15, H_2S removal, Regeneration

Introduction

Hydrogen sulphide is considered as one of the most noxious industrial gases for the atmosphere,[1-3] as well as a powerful catalyst poison in many processes,[4] and its concentration in feedstocks should be decreased to 10-100 ppb before their use.[5] To accomplish this task, ZnO-based sorbents have been successfully employed for decades in different domains of the chemical industry. In view of its high equilibrium constant for sulphidation, zinc oxide is still used both as pure phase or modified by adding other metals.[6,7] Given the large variety of process schemes, the optimum desulphurization temperature and the composition of the sorbents must be adapted correspondingly. Despite the differences in composition, the sorbents used in current industrial applications have similar textures, characterized by micrometer-sized particles. Utilization of unsupported nanostructured sorbents is not useful in these cases since nanoparticles would rapidly sinter at the high temperatures used during the sorption and/or regeneration steps. Moreover the gas-solid H_2S-oxide reaction occurs first at the surface and then extends to the bulk phase[8,9] often leaving an unreacted core.[10] A possible way for overcoming such drawbacks could be the dispersion of the active phase nanoparticles onto a suitable, high-surface area support.[11,12] The choice of supports able to strongly interact with the active phase seems inappropriate, as it could make difficult the regeneration of the spent sorbent.[13] Microporous supports, such as zeolites, seem inappropriate as well, due to the severe mass transfer limitations associated with their microporous system.[14] In view of the above, mesostructured SBA-15, an amorphous silica material with high surface area, regular channels and thick pore walls,[15] represents a promising support candidate.[16-18] In comparison with classical sorbents consisting of micrometer-sized particles, nanostructured oxides dispersed into the SBA-15 channels would be sintering-resistant and would hence exhibit a higher reactivity towards H_2S. Furthermore, the oxide/SBA-15 composite would behave as an ideal reactor, with the mesopores acting as channels for the rapid transport of the reactant.[19] Enhanced desulphurization activity of ZnO/SBA-15 nanocomposites prepared by different impregnation strategies has recently been demonstrated in the present authors' laboratory.[11] However, the slow kinetics of the reaction limits the sulphur loading capacity of ZnO-based sorbents. Iron oxide/SBA-15 nanocomposites could represent an interesting alternative as low-cost sorbents for H_2S removal in view of the rapid kinetics of H_2S reaction on iron oxide.[20-24] To the best of the present authors' knowledge, only one paper dealing with the use of SBA-15 as a support for iron oxide-based sorbents has been published so far.[25] In that work, an air stream containing a very low (0.1 vol.%) H_2S amount was contacted at room temperature with iron oxide-loaded SBA-15 samples. However, in most of the industrial applications significantly higher amounts of H_2S need to be removed from air-free hot gases, as for instance in the case of coal-, hydrocarbon- or biomass-derived syngas. In case of a low or ambient temperature cleanup step, the gases require reheating for downstream processing and it is apparent that if gasification, gas cleanup and downstream processing were carried out at nearly the same temperature the whole process would be more thermally efficient, *i.e.* both more economically viable and environmentally friendly. Besides such practical implications, fundamental reasons make iron oxide/SBA-15 composites worthy of being investigated in parallel with zinc oxide/SBA-15 sorbents for the mid- (300 °C) or high-temperature (> 500 °C) H_2S removal.

The present work deals with the synthesis and thorough characterization of both iron oxide/ and zinc oxide/SBA-15 composites, whose behaviour in the H_2S removal from gas streams was investigated at 300 °C with the aim of correlating the sorbents performance with their physico-chemical features. The sorbents with similar loading (16-18 wt.% of active phase) were prepared by the two-solvents hexane-water impregnation procedure.[11,26,27] The behaviour of the iron oxide/ and zinc oxide/SBA-15 composites in the removal of H_2S from an H_2S-He stream was investigated in a fixed-bed reactor and compared with that of an unsupported ZnO commercial sorbent. The morphological, structural and textural features of fresh, sulphided and regenerated sorbents were assessed by a multitechnique approach, including the study of the possible interactions between the guest oxide and the host silica support. Zinc oxide as well as iron oxide resulted highly dispersed into the well-ordered mesoporous silica channels under the form of a thin amorphous layer or of small nanoparticles. The efficient incorporation of the active phase into SBA-15 induced a considerable improvement of the desulphurization performance compared to the commercial sorbent. Temperature-programmed oxidation (TPO) runs were carried out on the sulphided sorbent samples aiming at shedding light on the changes undergone by the solid during regeneration treatments. The influence of repeated sorption-regeneration cycles on the sorbent features was also investigated.

Experimental

Preparation of SBA-15 mesostructured silica

SBA-15 mesoporous silica with a long-range-order structure was prepared using the neutral triblock copolymer Pluronic P123 ($EO_{20}PO_{70}EO_{20}$, Sigma Aldrich) as surfactant template, according to the procedure reported by Zhao.[15]

Preparation of sorbents

The MeO_x/SBA-15 sorbents were prepared via a “Two-Solvents” synthetic route.[11] 0.4 g of SBA-15 were first suspended in 12 cm^3 of *n*-hexane (first hydrophobic solvent) and stirred at 400 rpm for 15 min. 0.48 cm^3 of metal precursor ($Zn(NO_3)_2 \cdot 6H_2O$, Aldrich, 98%, 1 mmol or $Fe(NO_3)_3 \cdot 9H_2O$, Aldrich, 98%, 1 mmol) aqueous solution, corresponding to the SBA-15 pore volume previously determined by physisorption analysis (V_p = 1.2 cm^3/g), was then added drop-wise. The resulting dispersion was vigorously stirred for two hours at room temperature and then left to dry in air at 40 °C overnight. Finally, the dried product was calcined at 500 °C for 2 hours (heating rate 2 °C/min) to decompose the metal nitrates. The final metal oxide loading was assessed by Inductively Coupled Plasma Atomic Emission Spectrometry (ICP-AES) with a Varian Liberty 200 spectrophotometer. The active phase content resulted 18 and 16 wt.% for zinc oxide and iron oxide-based sorbent, respectively. The sorbent samples are labelled as Zn_*X* and Fe_*X*, where *X* denotes the state of the sorbent, F (Fresh), S (Sulphided) and R (Regenerated). Similar notation is used also for the commercial unsupported ZnO sorbent ($Katalco_{JM}$ 32-5).

Characterization of materials

Low-angle (2θ = 0.8-2.5°) and wide-angle (2θ = 10-70°) X-ray diffraction patterns were recorded on a Philips PanAnalytical X’Pert Pro diffractometer with a θ-θ Bragg Brentano geometry with Cu Kα wavelength. Low-angle diffraction patterns were recorded using a zero-background silicon sample holder. The coherent domain (crystallite size) was obtained by Scherrer’s equation using the Warren correction.[28] Transmission Electron Microscopy (TEM) investigation was carried out using a Jeol 200CX microscope operating at an accelerating voltage of 200 kV. High resolution transmission microscope (HRTEM) images were collected using a Jeol 2010 UHR equipped with a Gatan Imaging Filter (GIF) with a 15 eV window and a 794 slow scan CCD camera. Finely ground samples were dispersed in *n*-octane and subjected to an ultrasonic bath and the suspensions were then dropped on carbon-coated copper grids for the TEM and HRTEM observations. Textural analysis was carried out on a Sorptomatic 1990 System (Fisons Instrument) by determining the nitrogen adsorption/desorption isotherms at –196 °C. Prior to analysis, the samples were heated overnight under vacuum up to 220 °C (heating rate 1 °C/min). The Brunauer-Emmett-Teller (BET) specific surface area and pore volume were assessed from the adsorption data. The mean pore diameter was determined by applying the Barrett-Joyner-Halenda (BJH) model to the isotherm desorption branch.[29] FTIR spectra were collected using a Bruker Equinox 55 spectrophotometer at room temperature in the 400 to 4000 cm^{-1} region. The samples were analyzed dispersing the powders in KBr pellets. X-ray Photoelectron Spectroscopy analyses were performed by using an ESCALAB200 spectrometer manufactured by Vacuum Generator Ltd., East Grinstead, U. K. A non-monochromatic Al Kα X-ray source (1486.6 eV, 15 mA, 20 keV) was used and samples were analyzed as pellets. More details regarding the instrument configuration and data analysis are reported elsewhere.[30]

Desulphurization and regeneration activity evaluation of the sorbents

The desulphurization performance of the sorbents was evaluated at 300 °C by the breakthrough curves in a vertical quartz tubular reactor (10 mm I.D. x 20 mm length), coaxially located inside an electrical furnace. Quartz wool was used to support the sorbent bed (0.10 g) inside the reactor. Prior to the desulphurisation run, helium gas was fed into the reactor for 30 min at 300 °C in order to remove any water and/or impurities adsorbed on the sorbent surface. The H_2S-He reactant gas (1.5% H_2S, He balance) was then admitted (inlet flow rate 20 cm^3/min) and the H_2S uptake during the adsorption test was monitored using a quadrupole mass spectrometer (Thermo

Electron Corporation), where the detection limit of H_2S was about 50 ppm. When the H_2S concentration in the outlet gas reached 15000 ppmv, the inlet stream was stopped and helium was introduced to purge the system. The breakthrough capacity or Sulphur Retention Capacity (SRC), indicating the amount of sulphur retained per unit mass of sorbent, was determined when the outlet concentration of H_2S attained to 100 ppm by the formula

$$(SRC)\ \text{Sulphur retention capacity} = \frac{(F_s \cdot B_t)}{W}$$

where F_s represents the mass flow rate of sulphur (mg/s), B_t is the breakthrough time (s), and W indicates the sorbent weight (g), referred to either the pure active phase or the composite. After adsorption of H_2S the samples are referred to as "sulphided" (S) samples. The breakthrough time has been assessed by subtracting the blank from the experimental profiles.

TPO runs were carried out on a Thermo Electron 1100 TPD/R/O apparatus equipped with both a thermal conductivity detector (TCD) and a quadrupole mass spectrometer (QMS). The sulphided samples were heated under flowing air (20 cm^3/min) up to 500 °C (heating rate 10 °C/min) and hold for 4h.

Results and discussion

Desulphurization activity of fresh sorbents

Breakthrough curves for all the sorbents, the pure zinc oxide commercial sorbent (Katalco$_{JM}$ 32-5) included, were recorded at 300 °C (Fig. 1, ESI). No H_2S removal was detected for the bare SBA-15. For all the sorbents the values of breakthrough time and sulphur retention capacity (SRC), expressed relative to either the active phase content or to the total composite amount (active phase + support), are reported in Table 1. The incorporation of zinc or iron oxide into SBA-15 induces a considerable improvement of the SRC compared to the commercial sorbent. The highest retention capacity per unit mass of active phase is obtained for Fe_F (401 mg S/g Fe_2O_3), being more than seven-time higher than that of the Zn_F (53 mg S/g ZnO), and even much more higher than the corresponding value for the commercial zinc oxide sorbent (6 mg S/g ZnO). The by far superior performance of the SBA-15-supported sorbents with respect to that of the commercial sample can be reasonably ascribed to differences in the exposure of the active phase to the reactant H_2S. As reported in the following, though the surface area and the pore volume of the Fe_F are higher than that of the corresponding sorbent with zinc oxide, these textural properties cannot justify the tremendous enhancement of the SRC, since also differences in the intrinsic kinetics should be considered for explaining the sorption behaviour of Zn_F and Fe_F.

Fresh sorbents characterization

Fig. 1 shows the XRD patterns of Zn_F and Fe_F compared with that of the bare SBA-15 at low- (a) and wide-angle (b). The low-angle diffraction pattern of the SBA-15 support exhibits three observable reflections, indexable as (100), (110) and (200), which are characteristic of a two-dimensional highly ordered hexagonal arrangement of the channels (space group P6*mm*). The low-angle diffraction patterns of the sorbents also exhibit the three well-resolved diffraction peaks, which indicates that the organized pore structure is maintained despite the quite high active phase loading. A slight shift of the reflections towards higher angles can be observed for both sorbents, suggesting a small contraction of the cell parameters.

The wide-angle diffraction pattern of Zn_F (Fig. 1b) shows only the typical halo of amorphous silica at 2θ = *ca.* 23°. No diffraction peaks corresponding to ZnO phase are observable, indicating that the active phase is well dispersed into/over the support as an amorphous phase or as nanocrystals whose size is under the XRD detection limit. The pattern of Fe_F exhibits two further broad peaks at 2θ = 35.5° and 62.5° that can be attributed to the most intense reflections of maghemite-Fe_2O_3 phase (PDF Card 39-1346).

Fig. 2 shows the nitrogen adsorption-desorption isotherms (a) and the pore size distribution plots (b) of the fresh sorbents (Zn_F and Fe_F) in comparison with the bare SBA-15. The silica support exhibits a type IV isotherm with an H1 type hysteresis loop, characteristic of a mesoporous material with uniform cylindrical pores open at both ends.[31] The mesoporous character of the solid is preserved after the incorporation of the active phase, as revealed by the type IV shape of the isotherm for both the sorbents. A two-step desorption branch showing two inflection points at about $P/P_0 = 0.4$ and 0.6 is observed for Fe_F, in contrast with the case of Zn_F, whose hysteresis loop is rather similar to that of the parent SBA-15. The calculated values of surface area (S_{BET}) and pore volume (V_p) are reported in Table 2. For Zn_F, S_{BET} and V_p are much lower than the corresponding values of the bare support, which indicates partial filling of the mesopores by the metal oxide. Also for Fe_F the surface area and pore volume values are remarkably lower than those for the parent SBA-15. The pore size distribution plot for Zn_F (Fig. 2b) shows a narrow monomodal distribution centred at 6.2 nm. It is worthy of note that this value is slightly lower than that of SBA-15 (Fig. 2b). By subtracting the mean pore diameter from the unit cell parameter (a_0, calculated from low-angle XRD data), the wall thickness (T_w) values were calculated, resulting 5.0 and 5.2 nm for the bare SBA-15 and Zn_F, respectively (Table 2). Such a slight increase in the wall thickness as a consequence of ZnO deposition would be consistent with the presence of the oxide either as a layer or dispersed in clusters or very small nanoparticles. This is in agreement with the lack of ZnO reflections in the XRD pattern (Fig. 1b). At variance with the case of the zinc oxide-containing sorbent, Fe_F shows a bimodal pore size distribution (Fig. 2b) which seems related to the two-step feature observed in the desorption branch of the isotherm of this sample (Fig. 2a) and indicates that two distinct families of pores contribute to the overall pore volume. The family with wider size (maximum at 6.4 nm) is responsible for the hysteresis at $P/P_0 = 0.6$, typical of open-ended cylindrical mesopores, reasonably those pores of SBA-15 in which no deposition of iron oxide has occurred. The other pore family (maximum at 3.6 nm) can be associated with the hysteresis loop closing at relative pressure of *ca.* 0.4, which is suggestive of ink-bottle type mesopores, resulting from the iron oxide deposition: in the same pore, the volume between two oxide particles would be only accessible through a small neck. Similar features were also observed by other authors in the desorption branch of zirconia- and iron oxide-containing SBA-15.[32,33]

Representative TEM images of SBA-15, Zn_F and Fe_F are reported in Fig. 3. The well-ordered 2D-hexagonal symmetry of SBA-15 with regular empty mesochannels of *ca.* 6–7 nm in diameter and walls thickness of about 5 nm is clearly visible in Figs. 3a and 3b. TEM images of the Zn_F sorbent (Figs. 3c and 3d) do not show an evident variation if compared with bare SBA-15. No isolated ZnO particles are visible onto the external surface or inside the pores of Zn_F. This suggests that the formation of an amorphous and quite uniform thin layer of zinc oxide has occurred at the inner surface of the pore walls, in agreement with the XRD and BET data. At variance with the case of Zn_F, the Fe_F images (Figs. 3f and 3g) show that iron oxide is not uniformly dispersed; note the rough contours of the channels (some of which appear completely filled) resulting by the deposition of the oxide nanoparticles. The crystalline nature of these nanoparticles is revealed by the high resolution micrograph in the inset of Fig. 3f, where the calculate *d* spacing (0.25 nm) is in agreement with the (311) reflection of maghemite (PDF Card 39-1346).

The different outcome of the oxide deposition process in the case of Zn_F and Fe_F could be justified by the different affinity of the zinc and iron cations for the silica host. According to the literature,[34-36] silica depolymerization can occur in the presence of ZnO phases even at low treatment temperature, due to the occurrence of silanol groups-oxide phase interaction. By converse, no interaction between silanols and the oxide phase was observed for a Fe_2O_3-SiO_2 nanocomposite.[37] Accordingly, the formation of the homogeneous zinc oxide nanolayer at the internal surface of the pores of Zn_F would be triggered by the above-cited interactions, whereas their lack would lead to nanoparticles deposition in the case of Fe_F.

In view of the possible role of the host-guest interactions in determining the final active phase dispersion, which in turn would influence the performance of the sorbents, the latter were also investigated by FTIR. The spectra of the sorbents are reported in Fig. 4 and compared with the spectrum of the bare SBA-15. Most of the features are common to all the spectra: (i) the absorption bands at 1200-1080 and 800 cm^{-1} of the asymmetric and symmetric modes of Si-O-Si groups, respectively;[38] (ii) the absorption band at 960 cm^{-1} of Si-OH stretching modes of the non-condensed Si-OH groups and the band at 465 cm^{-1} due to bending of the O-Si-O groups; (iii) the absorption peak at around 1630 cm$^{−1}$ of the H-O-H bending vibration of H_2O adsorbed in capillary pores and on the surface. For both the sorbents, the absence of the typical narrow signal around 1370 cm$^{−1}$ due to the stretching vibration of the NO_3^- groups proves the complete decomposition of nitrates. Interestingly, the band at 960 cm^{-1} is still clearly visible after the incorporation of the iron oxide phase, whereas it is absent in the case of Zn_F sorbent, which provides further evidence for the occurrence of interactions between the ZnO phase and the silica matrix.

Further confirmation of this interaction is obtained by XPS analyses: Zn2p$_{3/2}$ signal of Zn_F sorbent (Fig. 5a) shows a single component at 1022.7 ± 0.2 eV while the kinetic energy of the Auger ZnLMM peak was found to be 986.3 ± 0.2 eV. These values indicate the formation of Si-O-Zn bonds, in agreement with the findings of other authors.[39] Such interactions, which are responsible for the deposition of zinc oxide as an amorphous thin layer at the surface of the SBA-15 channels, also make the zinc oxide phase differently available to react with the hydrogen sulphide, in comparison with the case of iron oxide nanoparticles not interacting with the host matrix.

As far as iron is concerned, in Fe_F sorbent XPS Fe2p$_{3/2}$ spectrum (Fig. 5b) shows only the presence of two components at 710.3 ± 0.2 eV and 711.6 ± 0.2 eV which can be assigned to Fe (III) in Fe_2O_3 and FeOOH respectively.[40]

Sulphided sorbents characterization

The low-angle diffraction patterns of the sulphided sorbents show that the characteristic hexagonal order is preserved in all the samples (Fig. 1a). Only in the pattern of Zn_S, the (100), (110) and (200) peaks significantly shift towards higher angles than those of the Zn_F pattern, suggesting a slight shrinkage in the mesoporous framework. The wide-angle XRD patterns of the sulphided sorbents (Fig. 1b) show that for Zn_S, in addition to the broad halo related to amorphous silica, broad and intense reflections at 28.6°, 47.7° and 56.6° are present, assigned to ZnS phase (PDF Card 12-688). The mean size of the ZnS nanocrystals can be estimated in the 3-4 nm range. The broadening of the reflections does not permit to exclude the presence of an amorphous sulphided phase. A small peak centred at about $2\theta = 33°$ is observed in the pattern of Fe_S, attributed to the most intense reflection (101) of the FeS_2 pyrite phase (PDF Card 71-2219). A large band overlapping with the main reflection of pyrite phase could suggest the possible presence of an amorphous iron sulphide phase; the presence of unreacted maghemite cannot be excluded.

Nitrogen physisorption isotherms (Fig. 2c) confirm the mesostructured character of the sulphided sorbents. As a consequence of the sulphidation process, zinc oxide is transformed into ZnS. Due to the different molar volume values of ZnO (15.07 cm^3/mol) and ZnS (24.3 cm^3/mol) an expansion in the volume of the guest material as high as 38% should be expected in case of complete ZnO/ZnS conversion. Such expansion should lead to a decrease in surface area and pore volume, which is actually observed (Table 2). The occurrence of an increase in the guest phase volume is also confirmed by the monomodal pore size distribution centred at 3.8 nm observed for the sulphided sorbent (Fig. 2d). Note (Table 2) that the wall thickness (T_w) value is significantly higher than the value for Zn_F. Due to the nanocrystalline nature of the ZnS phase, and the increased electronic density contrast in comparison with zinc oxide, it is possible to point out in TEM micrographs (Fig. 3e) that the particles are mainly anchored at the channel walls, whose contours appear rather rough, with a rope-like profile. The image at higher magnification (Fig. 3e, inset), shows that, in agreement with the wide-angle XRD results, the ZnS nanoparticles are 3-4 nm wide. HRTEM image, reported as inset of Fig. 3e, shows two nanoparticles with *d* spacing values of 0.31 and 0.33 nm which are in agreement with the (0010) and (100) reflections of hexagonal ZnS phase (PDF Card 12-688) respectively.

Based on the sulphidation reaction stoichiometry, the conversion of Fe_2O_3 (30.71 cm^3/mol) into FeS_2 (51.06 cm^3/2 mol) would be accompanied by an expansion in the volume of the guest material and as a consequence in the lowering of surface area of the composite. The observed surface area and pore volume values for Fe_S are actually slightly lower than that for Fe_F (Table 2). The bimodal pore size distribution (Fig. 2d) is maintained in the sulphided sample, and that the second peak in the pore size distribution of Fe_S is centred at 6.0 nm, *i.e.* slightly lower than that for Fe_F, in agreement with the presence of iron sulphide phase occupying the pores. No significant differences between the fresh and sulphided sorbent are visible in the TEM micrographs for these samples (*cf.* Figs. 3f and 3h).

The FTIR spectra of the sulphided sorbents are provided in Fig. 4. A comparison between the spectra for Zn_F and Zn_S reveals that in the latter the Si-OH band at 960 cm^{-1} reappears, hence suggesting that the Zn-containing phase formed upon sulphidation does not interact significantly with the silica surface. Interestingly, this occurs simultaneously with the transformation of the amorphous zinc oxide phase into a crystalline ZnS phase, evidenced by the wide-angle XRD patterns (Fig. 1b). By contrast, in Fe_S the band at 960 cm^{-1} is strongly attenuated, suggesting that interactions between the silica host and the iron sulphide guest phase take place to a remarkable extent. It is worthy of note that this is accompanied by the loss of the crystalline character of the iron oxide as a consequence of its transformation into the sulphided phase (*cf.* Fig. 1b). The presence of FeS_2 phase, revealed by both the XRD pattern and the *pale brass-yellow* color of Fe_S, can be responsible for the low-intensity band at 600 cm^{-1} in agreement with Philias.[41] The pyrite formation is also consistent with the thermodynamic stability of this phase in comparison with the other iron sulphides.

The formation of both ZnS and FeS_2 is confirmed by XPS analyses. $Zn2p_{3/2}$ signal (Fig. 5a) shows, together with the component at 1022.7 eV due to Zn involved in Si-O-Zn bonds, a component at lower binding energy values (1021.9 ± 0.2 eV) which can be assigned to ZnS. In $Fe2p_{3/2}$ signal (Fig. 5b) a component at 707.2 eV ± 0.2 eV, due to pyritic iron is observed.[42] Sulphur

S2p peaks of both Fe_S and Zn_S sorbents show a single component at 162.5 eV and at 162.0 eV respectively (Fig. 5c) that could be assigned to sulphur in pyrite and in ZnS respectively.[43] Further confirmation of the presence of FeS_2 and ZnS at the sorbent surfaces is obtained by stoichiometry calculated from XPS data: the ratio between pyritic iron and sulphur is found to be 0.45 while the ratio Zn/S, calculated taking into account only the lower binding energy component of the zinc signal, is 1.10. All these results are in good agreement with XRD analysis for both sorbents.

Sorbents regeneration

Since the sorbent regeneration determines its usable lifetime, temperature-programmed oxidation experiments were carried out on the sulphided samples. In preliminary runs a thermal conductivity detector (TCD) was used to monitor the effluent stream from the sample heated under flowing air (20 cm^3/min) up to 500 °C (heating rate 10 °C/min) and hold for 4 h, heated again up to 700 °C and hold for 1 h. The TCD profiles (Fig. 2, ESI) showed for Fe_S the presence of some peaks in the temperature region not exceeding 500 °C, no further peaks being detected above such temperature. By converse, in the case of Zn_S, besides a large peak at 500 °C another peak was observed at 690 °C. It is worthy of note that for temperatures $\leq$ 500 °C the oxidation of the sulphided commercial sample was almost negligible, only a very low, enlarged signal being detected for such temperatures in the TCD profile; heating of the sample well above 500 °C was required for the onset of oxidation to a significant extent.

As the TCD signal does not give information about the species by which the single contributions originate, further runs were carried out in which the SO_2 and O_2 species in the outlet gas composition were simultaneously monitored by quadrupole mass spectrometer (QMS). All these runs were carried out at a temperature not exceeding 500 °C, in view of the detrimental effect of higher temperatures on the SRC of ZnO/SBA-15 sorbents.[11] Another reason for such choice stems from previous ^{29}Si MAS-NMR experiments,[34] which revealed that the thermal treatment of sol–gel ZnO–SiO_2 nanocomposites in the 500-700 °C range induces the depolymerization of the host matrix and the possible formation of zinc silicates as a consequence of its interaction with zinc oxide. Fig. 6 reports both the TCD and QMS signals for Fe_S. The TCD profile shows a peak at 185 °C, a broad contribution at 260 °C, as well as two well-resolved peaks at 322 °C and 345 °C. The QMS profiles for O_2 and SO_2 reveal that the peak at 185 °C and the broad contribution at 260 °C are due to O_2 consumption and SO_2 release, respectively. A second O_2 consumption step is responsible for the narrow signal at 322 °C which correlates with the successive release of a considerable SO_2 amount at 345 °C. The two different O_2 consumption steps and subsequent SO_2 formation steps are ascribable to the presence of two different sulphided species, one of which is reasonably the crystalline pyrite phase revealed by XRD. Inspection of the TCD and QMS profiles for Zn_S (Fig. 7) shows that both the unresolved TCD peak at 322 °C and the large peak at 500 °C stem from an O_2 consumption and the associated SO_2 release. One of these two steps of Zn_S oxidation corresponds to the oxidation of a crystalline ZnS phase (whose presence was revealed by XRD) while the other could be ascribed to the oxidation of a zinc sulphide amorphous phase not visible by XRD.

Desulphurization-regeneration cycles and regenerated sorbents characterization

Repeated sorption-regeneration cycles were carried out in order to investigate the desorption behaviour and the stability of the regenerated sorbents. From the breakthrough curves (Figs. 8a and 8b), the B_t and SRC values for all the sorbents were obtained. These are reported in Table 3. The regeneration process is unable to restore a significant sorption activity for the ZnO commercial sample, both the breakthrough time and the sulphur retention capacity of the regenerated sample (2 mg S/g ZnO *vs.* 6 mg S/g ZnO of the fresh sorbent) being dramatically lower than those of the fresh sorbent. By converse, an enhanced performance of the regenerated sample in comparison with the fresh one is observed for the ZnO-based sorbent (68 mg S/g ZnO *vs.* 53 mg S/g ZnO of the fresh sorbent). For the iron oxide-based sorbent the regeneration process results in the partial recovering of the original sorption activity (199 mg S/g Fe_2O_3 *vs.* 401 mg S/g Fe_2O_3 of the fresh sorbent), the

B_t and SRC values for the regenerated sorbent being nearly halved in comparison with Fe_F. No further significantly changes in the sorption behaviour are observed for any of the sorbents upon repeating the sorption-regeneration cycle. The superior features of the iron oxide-based sorbent are worthy of note: the breakthrough time and the sulphur retention capacity of the regenerated sample are far higher than those of the ZnO-based sorbent, both under the fresh or regenerated form.

The poor performance of the regenerated commercial sample is not unexpected, as the TPO results showed that a thermal treatment well above 500 °C was required to convert the ZnS phase into the active oxide phase.

Concerning the regenerated zinc oxide-based sorbent, it results quite similar to the fresh one, as observed by XRD patterns (Fig. 3, ESI) and the FTIR spectra (Fig. 4, ESI). According to Table 2 data, the surface area of Zn_R is significantly lower than that of Zn_F. Despite this, a better performance is observed on the former. Such enhancement in the sorption activity of the zinc oxide-based composite in cycle operation is in agreement with the findings of a previous work on ZnO/SBA-15 sorbents with lower (10 wt.%) and higher (30 and 60 wt.%) zinc oxide content.[11] No simple correlation exists between the accessibility parameters (S_{BET} and V_p) and the sorbent performance. Based on the evidences of the previous work, it can be suggested that the ZnO phase originating from the ZnS oxidation during the regeneration step of the sorbent is different in terms of crystallinity, particle size and texture from the one obtained directly by thermal decomposition of the zinc nitrate precursor, *i.e.* that the regeneration process induces a reorganization of the zinc oxide nanophase.

For the iron oxide-based sorbent, a decrease in surface area occurs as a consequence of the regeneration process (Table 2), but the difference (15 %) seems too slight for explaining the observed halving of the B_t and SRC values. At variance with the case of ZnO/SBA-15 sorbent, the XRD and FTIR techniques are able to reveal differences between the regenerated and fresh iron oxide/SBA-15 samples. After regeneration the XRD reflections attributable to the sulphided phases disappear and diffraction peaks ascribable to maghemite phase are observed (Fig. 3, ESI), though weaker and slightly broader than for Fe_F. This can be due to either a lower amount of maghemite phase or differences in its crystallinity, owing to a decrease in the crystalline domain size and/or accumulated strain. In the FTIR spectrum of Fe_R sorbent (Fig. 4, ESI), the Si-OH band at 960 cm^{-1} is less intense than that observed in the fresh sorbent, which suggests the occurrence on the former of weak interactions between the guest phase and the silica matrix. Interestingly, two low-intensity signals at about 470 cm^{-1} and 610 cm^{-1} are observable, which indicate the presence of an iron sulphate phase, not revealed in the XRD pattern.

For better understanding of the changes undergone by the sorbent during the sulphidation-regeneration cycles, the investigation was extended to a pure nanostructured maghemite phase, which was first sulphided and then regenerated. The corresponding XRD patterns (Fig. 5, ESI) showed for the sulphided sample the presence of pyrrhotite ($Fe_{1-x}S$) and pyrite (FeS_2), as well as of a minor amount of unreacted maghemite. The absence in the sulphided composite of the pyrrhotite phase can be probably due to its metastability, enhanced by the nanodispersed nature of the sulphide. Interestingly, besides a remarkable amount of maghemite, the presence of iron sulphate ($Fe_2(SO_4)_3$) was detected by XRD after regeneration by heating at 500 °C and holding for 4 h. After heating up to 700 °C, no sulphate phase was detected in the XRD pattern where only maghemite phase was present. According to the above, the incomplete recover of the sorption activity of the iron oxide/SBA-15 composite after the sorption-regeneration cycles can be ascribed to the presence of iron sulphate, which is inert towards H_2S. Such iron sulphate phase is not visible in Fig. 3 of ESI because of the overlapping of its most intense peaks with the broad silica band at $2\theta = ca.\ 23°$.

The different behaviour of the regenerated sorbents in comparison with the fresh ones can hence be ascribed to different factors. In the case of the zinc oxide-based sorbent an increase in crystallinity of the ZnO phase originating from the ZnS oxidation during the regeneration step with respect to the crystallinity of the phase obtained directly by thermal decomposition of the zinc nitrate precursor would be responsible for the enhanced performance of the regenerated sorbent. In the case of the iron oxide-based sorbent the formation, during the regeneration step, of an iron sulphate phase unable to react with H_2S would explain the lack of complete recovery of the sorption capacity of the regenerated sorbent.

Conclusions

A simple, reproducible and easy-to-scale-up two-solvents incipient impregnation route has been used for dispersing zinc oxide and iron oxide inside the mesoporous channel system of SBA-15. The resulting nanocomposites have a remarkable performance for the H_2S removal from hot (300 °C) gas streams, the activity of the zinc oxide and the iron oxide systems being seven and seventy times higher than that of an unsupported zinc oxide commercial sorbent, respectively. The zinc oxide phase is incorporated as a thin amorphous homogeneous layer while the iron oxide one is dispersed in form of small maghemite crystallites. Differences in the morphology and the crystallinity of the active phase, as well as in the textural features of the composites, seem related to the lack or presence of interactions between the guest oxide phase and host silica matrix, which in turn make the iron oxide and zinc oxide phases differently prone to react with hydrogen sulphide. After regeneration of the sulphided sample, the sorption properties of the zinc oxide/SBA-15 composite appear enhanced and are maintained upon repeating the sorption-regeneration cycle. The iron oxide/SBA-15 sorbent shows the highest sulphur retention capacity. Its performance significantly decreases at the second sorption cycle mainly due to the formation of an iron sulphate phase, but is retained at the third sorption cycle. This indicates that the amount of H_2S-inert iron sulphate does not increase further. Noteworthy, though decreased in comparison with that of the fresh sample, the performance of the regenerated iron oxide-based sorbent is still far better than that of the ZnO-based one, either fresh or regenerated. The oxidation step for obtaining the regenerated iron oxide-based sorbent can be carried out at $T \leq 350$ °C, which is considerably lower than that required in the case of the ZnO-based sample. In view of a possible application, this would be quite important for the thermal efficiency of the sorption-regeneration process.

Acknowledgements

Consorzio AUSI (Consorzio per la promozione delle Attività Universitarie del Sulcis-Iglesiente) is gratefully acknowledged for Mauro Mureddu PhD grant financing. This work was also supported by ENEA (Italian National Agency for New Technologies, Energy and Sustainable Economic Development). The use of HRTEM facilities of C.G.S. (Centro Grandi Strumenti, University of Cagliari) is gratefully acknowledged. Thanks are due to MIUR (Italian Ministry of University and Research) for the fellowships of A. Ardu. Sardinian Regional Government is gratefully acknowledged for the financial support (P.O.R. Sardegna F.S.E. Operational Program of the Regione Autonoma della Sardegna, European Social Fund 2007-2013- Axis IV Human Resources, Objective 1.3, Line of Activity 1.3.1 "Avviso di chiamata per il finanziamento di Assegni di Ricerca".

References

1 D. Stirling and J. H. Clark, in *The Sulfur Problem: Cleaning Up Industrial Feedstocks*, RSC, 2000, pp. 16-30, DOI:10.1039/9781847552174-00016.

2 U. M. Cowgill, *Stud. Environ. Sci.*, 1984, **25**, 233.

3 O. Badr and S. D. Probert, *Appl. Energy*, 1994, **47**, 1.

4 P. Dhage, A. Samokhvalov, D. Repala, E. C. Duin and B. J. Tatarchuk, *Phys. Chem. Chem. Phys.*, 2011, **13**, 2179.

5 A. Samokhvalov and B. J. Tatarchuk, *Phys. Chem. Chem. Phys.*, 2011, **13**, 3197.

6 T. Baird, K. C. Campbell, P. J. Holliman, R. W. Hoyle, M. Huxam, D. Stirling, B. P. Williams and M. Morris, *J. Mater. Chem.*, 1999, **9**, 599.

7 H. F. Garces, A. E. Espinal and S. L. Suib, *J. Phys. Chem. C*, 2012, **116**, 8465.

8 S. P. Hernandez, M. Chiappero, N. Russo and D. Fino, *Chem. Eng. J.*, 2011, **176-177**, 272.

9 P. V. Ranade and D. P. Harrison, *Chem. Eng. Sci.*, 1981, **36**, 1079.

10 J. B. Gibson and D. P. Harrison, *Ind. Eng. Chem. Proc. Des. Dev.*, 1980, **19**, 231.

11 M. Mureddu, I. Ferino, E. Rombi, M. G. Cutrufello, P. Deiana, A. Ardu, A. Musinu, G. Piccaluga and C. Cannas, *Fuel*, 2012, **102**, 691.

12 D. Montes, E. Tocuyo, E. González, D. Rodríguez, R. Solano, R. Atencio, M. A. Ramos and A. Moronta, *Micropor. Mesopor. Mat.*, 2013, **168**, 111.

13 T. H. Ko, H. Chu and L. K. Chaung, *Chemosphere*, 2005, **58**, 467.

14 C. L. Hwang and N. H. Tai, *Appl. Catal. B*, 2010, **93**, 363.

15 D. Zhao, J. Feng, Q. Huo, N. Melosh, G. H. Fredrikson, B. F. Chmelka and G. D. Stucky, *Science*, 1998, **279**, 548.

16 C. Vogt, G. P. Knowles and A. L. Chaffee, *J. Mater. Chem. A*, 2014, **2**, 4299.

17 F. M. Zhang, B. S. Liu, Y. Zhang, Y. H. Guo, Z. Y. Wan and F. Subhan, *J. Hazard. Mater.*, 2012, **233-234**, 219.

18 B. S. Liu, X. N. Wei, Y. P. Zhan, R. Z. Chang, F. Subhan and C. T. Au, *Appl. Catal. B: Environ.*, 2011, **102**, 27.

19 J. A. Melero, G. Calleja, F. Martìnez and R. Molina, *Catal. Commun.*, 2006, **7**, 478.

20 P. J. H. Carnell and P. E. Starkey, *Chem. Eng.*, 1984, **408**, 30.

21 J. A. Rodriguez, S. Chaturvedi, M. Kuhn and J. Hrbek, *J. Phys. Chem. B*, 1998, **102**, 5511.

22 A. Davydov, K. T. Chuang and A. R. Sanger, *J. Phys. Chem. B*, 1998, **102**, 4745.

23 S. S. Tamhankar and C. Y. Wen, *Ind. Gas Sep.*, 1983, **223**, 255.

24 J. Deng, J. Ma, L. Mei, Y. Tang, Y. Chen, T. Lv, Z. Xu and T. Wang, *J. Mater. Chem. A*, 2013, **1**, 12400.

25 X. Wang, J. Jia, L. Zhao and T. Sun, *Water Air Soil Pollut.*, 2008, **193**, 247.

26 J. van der Meer, I. Bardez-Giboire, C. Mercier, B. Revel, A. Davidson and R. Denoyel, *J. Phys. Chem. C*, 2010, **114**, 3507.

27 F. Boubekr, A. Davidson, S. Casale and P. Massiani, *Micropor. Mesopor. Mat.*, 2011, **141**, 157.

28 H. P. Klug and L. E. Alexander in *X-Ray diffraction procedures: For polycrystalline and amorphous materials*, ed. John Wiley & Sons, Inc., New York, 1954, ch. 9, pp. 491-538.

29 E. P. Barret, L. G. Joyner and P. P. Halenda, *J. Am. Chem. Soc.*, 1951, **73**, 373.

30 M. Fantauzzi, A. Rigoldi, B. Elsener, D. Atzei and A. Rossi, *J. Electron Spectrosc. Relat. Phenom.*, 2014, **193**, 6.

31 F. Rouquerol, J. Rouquerol and K. Sing, in *Adsorption by Powders and Porous Solids*, Academic Press, 1999, ch. 7, pp. 191-217.

32 A. H. Jansen, C. M. Yang, Y. Wang, F. Schüth, A. J. Koster and K. P. de Jong, *J. Phys. Chem. B*, 2003, **107**, 10552.

33 E. Delahaye, V. Escax, N. El Hassan, A. Davidson, R. Aquino, V. Dupuis, R. Perzynski and Y. L. Raikher, *J. Phys. Chem. B*, 2006, **110**, 26001.

34 C. Cannas, M. Casu, A. Lai, A. Musinu and G. Piccaluga, *J. Mater. Chem.*, 1999, **9**, 1765.

35 Q. Jiang, Z. Y. Wu, Y. M. Wang, Y. Cao, C. F. Zhou and J. H. Zhu, *J. Mater. Chem.*, 2006, **16**, 1536.

36 R. Anedda, C. Cannas, A. Musinu, G. Pinna, G. Piccaluga and M. Casu, *J. Nanopart. Res.*, 2008, **10**, 107.

37 S. Bruni, F. Cariati, M. Casu, A. Lai, A. Musinu, G. Piccaluga and S. Solinas, *Nanostruct. Mater.*, 1999, **11**, 573.

38 A. Bertoluzza, C. Fagnano, M. A. Morelli, V. Gottardi and M. Guglielmi, *J. Non-Cryst. Solids,* 1982, **48**, 117.

39 Q. Jiang, Z. Y. Wu, Y. M. Wang, Y. Cao, C. F. Zhou and J. H. Zhu, *J. Mater. Chem.*, 2006, **16**, 1536.

40 M. Fantauzzi, A. Pacella, D. Atzei, A. Gianfagna, G. B. Andreozzi and A. Rossi, *Anal. Bioanal. Chem.*, 2010, **396**, 2889.

41 J. M. Philias and B. Marsan, *Electrochimica Acta*, 1999, **44**, 2351.

42 M. Fantauzzi, C. Licheri, D. Atzei, G. Loi, B. Elsener, G. Rossi and A. Rossi, *Anal. Bioanal. Chem.*, 2011, **401**, 2237.

43 M. Fantauzzi, D. Atzei, B. Elsener, P. Lattanzi and A. Rossi, *Surf. Interface Anal.*, 2006, **38**, 922.

Tables

Table 1. Breakthrough time (B_t) and Sulphur Retention Capacity (SRC) of fresh zinc oxide- and iron oxide-based sorbents. Data for the ZnO commercial sorbent (Katalco$_{JM}$ 32-5) are also reported for comparison.

Sample	B_t (s)	SRC ($mg_S/g_{active\ phase}$)	SRC ($mg_S/g_{sorbent}$)
Katalco$_{JM}$_F	103	6	6
Zn_F	180	53	10
Fe_F	1350	401	80

Table 2. N_2 physisorption data of fresh, sulphided and regenerated zinc oxide- and iron oxide-based sorbents compared with the bare SBA-15 and the ZnO commercial sorbent (Katalco$_{JM}$ 32-5). The thickness of the pore walls (T_w) is also reported.

Sample	S_{BET} (m^2/g)	V_p (cm^3/g)	D_p (nm)	T_w (nm)
Bare SBA-15	770	1.20	6.4	5.0
Katalco$_{JM}$_F	9	0.10	-	-
Zn_F	482	0.90	6.2	5.2
Zn_S	406	0.76	3.8	7.2
Zn_R	332	0.69	5.4	
Fe_F	545	0.87	3.6 ; 6.4	-
Fe_S	525	0.84	3.9 ; 6.0	-
Fe_R	463	0.80	3.5 ; 6.0	-

S_{BET}: BET Specific Surface Area; V_p: Pore Volume; D_p: Pore Diameter; T_w: Wall Thickness = (a_0 - D_p); a_0: XRD unit cell parameter. Relative Standard Deviation: %RSD (S_{BET}) = 2.1%; %RSD (V_p) = 1.1%; %RSD (D_p) = 1.8%.

Table 3. Breakthrough time (B_t) and Sulphur Retention Capacity (SRC) of fresh and regenerated zinc oxide- and iron oxide-based sorbents during sorption-regeneration cycles. Data for the commercial Katalco$_{JM}$ 32-5 sorbent are also reported for comparison.

Sample	**Run number**[a]	**B_t (s)**	**SRC ($mg_S/g_{Active\ phase}$)**	**SRC ($mg_S/g_{Sorbent}$)**
Katalco$_{JM}$_F	1	103	6	6
Katalco$_{JM}$_R	2	26	2	2
Katalco$_{JM}$_R	3	26	2	2
Zn_F	1	180	53	10
Zn_R	2	230	68	13
Zn_R	3	250	74	14
Fe_F	1	1350	401	80
Fe_R	2	670	199	40
Fe_R	3	710	211	42

[a] 1= Fresh sorbent; 2 = after 1st regeneration; 3 = after 2nd regeneration

Figure Captions

Figure 1. XRD patterns of bare SBA-15, zinc oxide- and iron oxide-based sorbents in the fresh and sulphided state at low-angle (a) and wide-angle (b). The main reflection planes are marked.

Figure 2. Nitrogen adsorption-desorption isotherms (a and c) and pore size distribution (b and d) of bare SBA-15, zinc oxide- and iron oxide-based sorbents in the fresh and sulphided state (full circles bare SBA-15, empty circles Zn_F and Zn_S, full squares Fe_F and Fe_S).

Figure 3. Representative TEM images of: bare SBA-15 viewed along (a) and perpendicular (b) to the axis of the hexagonal arranged mesopores; Zn_F (c and d); Zn_S (e); Fe_F (f and g); Fe_S (h).

Figure 4. FTIR spectra of bare SBA-15, zinc oxide- and iron oxide-based sorbents in the fresh (F) and sulphided state (S).

Figure 5. $Zn2p_{3/2}$ (a) and $Fe2p_{3/2}$ (b) XPS spectra of fresh and sulphided sorbents. (c) S2p XPS signals of Fe_S and Zn_S sorbents.

Figure 6. TPO profile and SO_2 and O_2 quadrupole mass spectrometer (QMS) signals of the Fe_S sulphided sorbent regenerated at 500 °C.

Figure 7. TPO profile and SO_2 and O_2 quadrupole mass spectrometer (QMS) signals of the Zn_S sulphided sorbent regenerated at 500 °C.

Figure 8. H_2S breakthrough curves upon three sorption-regeneration cycles (S1, S2, S3) for the zinc oxide-based sorbent (a) and iron oxide-based sorbent (b).

Figures

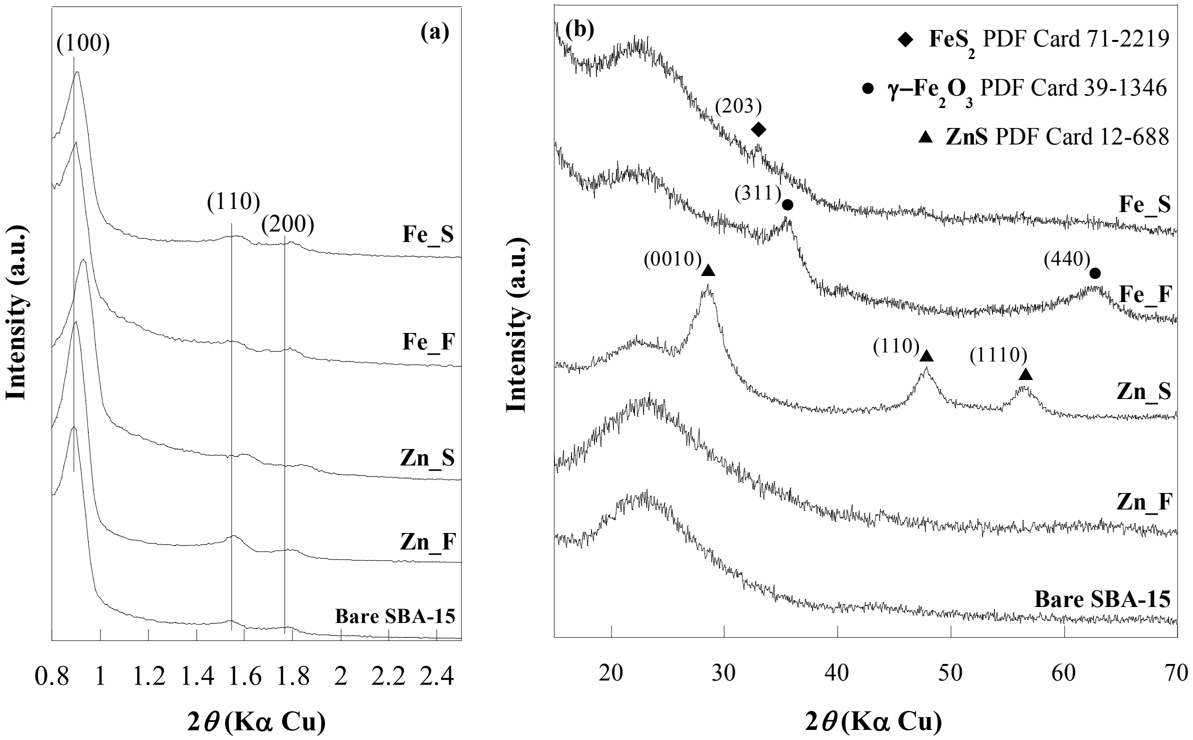

Figure 1

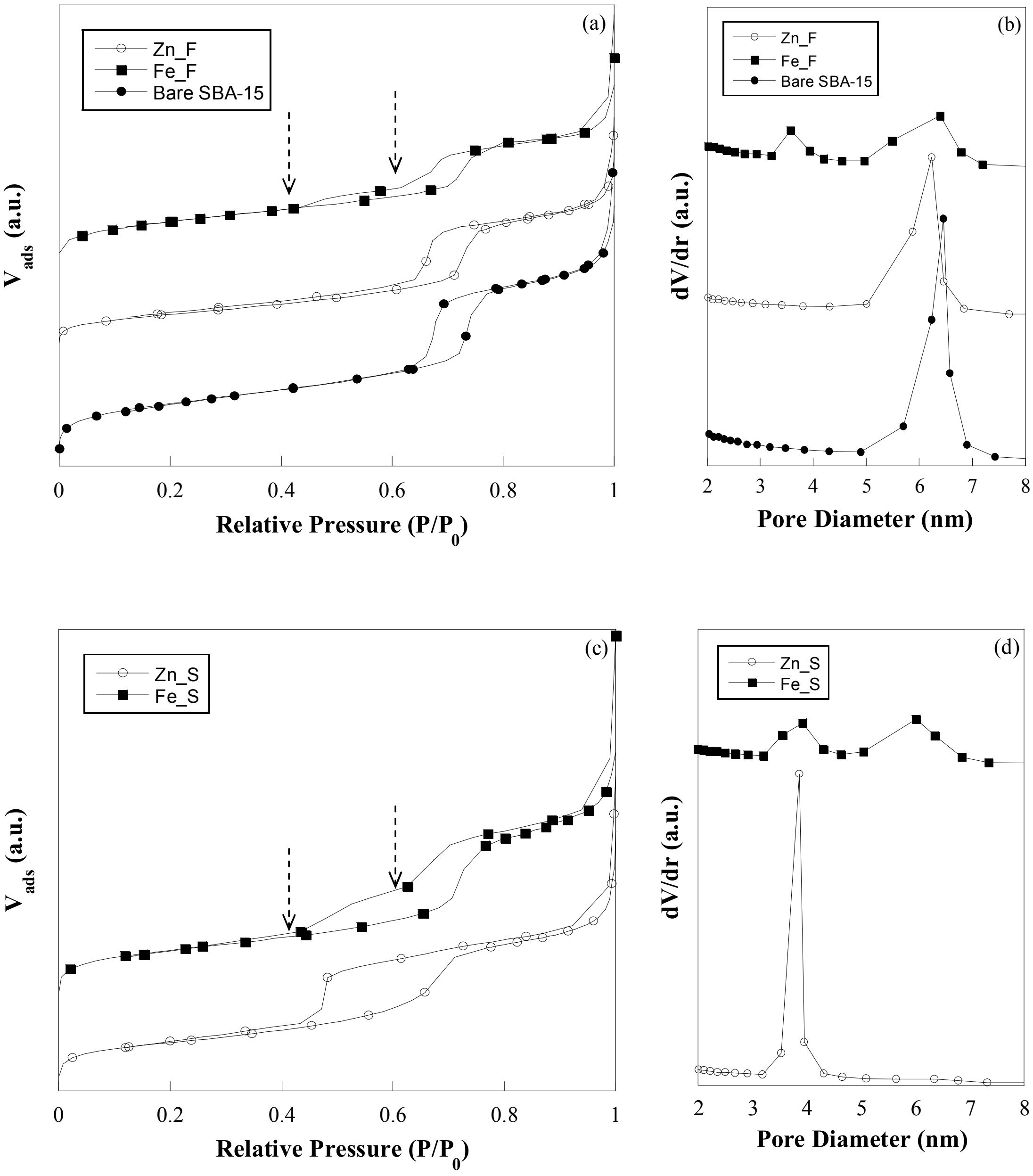
(a)
Zn_F
Fe_F
Bare SBA-15
V_ads (a.u.)
0
0.2
0.4
0.6
0.8
1
Relative Pressure (P/P0)
(b)
Zn_F
Fe_F
Bare SBA-15
dV/dr (a.u.)
2
3
4
5
6
7
8
Pore Diameter (nm)
(c)
Zn_S
Fe_S
V_ads (a.u.)
0
0.2
0.4
0.6
0.8
1
Relative Pressure (P/P0)
(d)
Zn_S
Fe_S
dV/dr (a.u.)
2
3
4
5
6
7
8
Pore Diameter (nm)

Figure 2

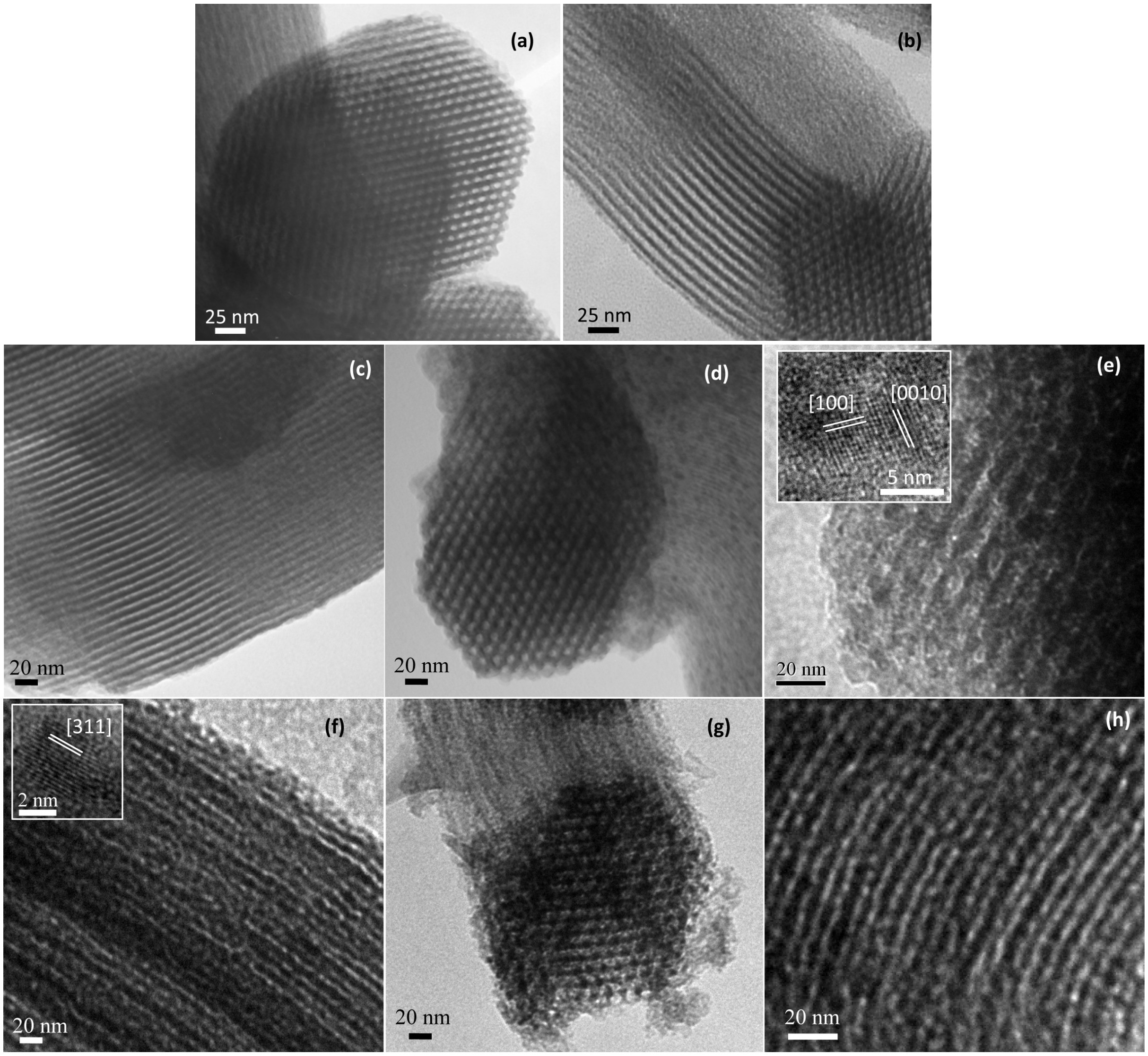
(a)
25 nm
(b)
25 nm
(c)
20 nm
(d)
20 nm
(e)
[100]
[0010]
5 nm
20 nm
(f)
[311]
2 nm
20 nm
(g)
20 nm
(h)
20 nm

Figure 3

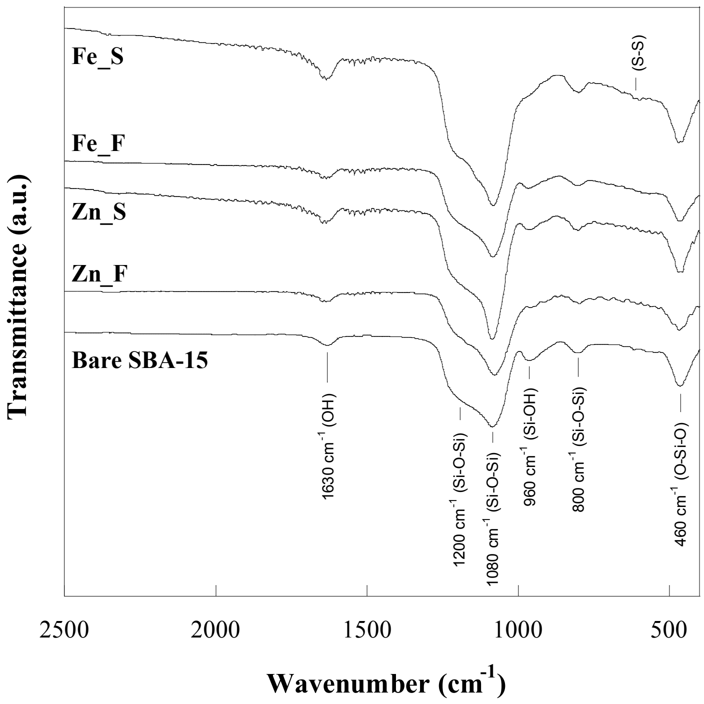
Fe_S
(S-S)
Fe_F
Zn_S
Zn_F
Bare SBA-15
1630 cm-1 (OH)
1200 cm-1 (Si-O-Si)
1080 cm-1 (Si-O-Si)
960 cm-1 (Si-OH)
800 cm-1 (Si-O-Si)
460 cm-1 (O-Si-O)
Transmittance (a.u.)
2500
2000
1500
1000
500
Wavenumber (cm-1)

Figure 4

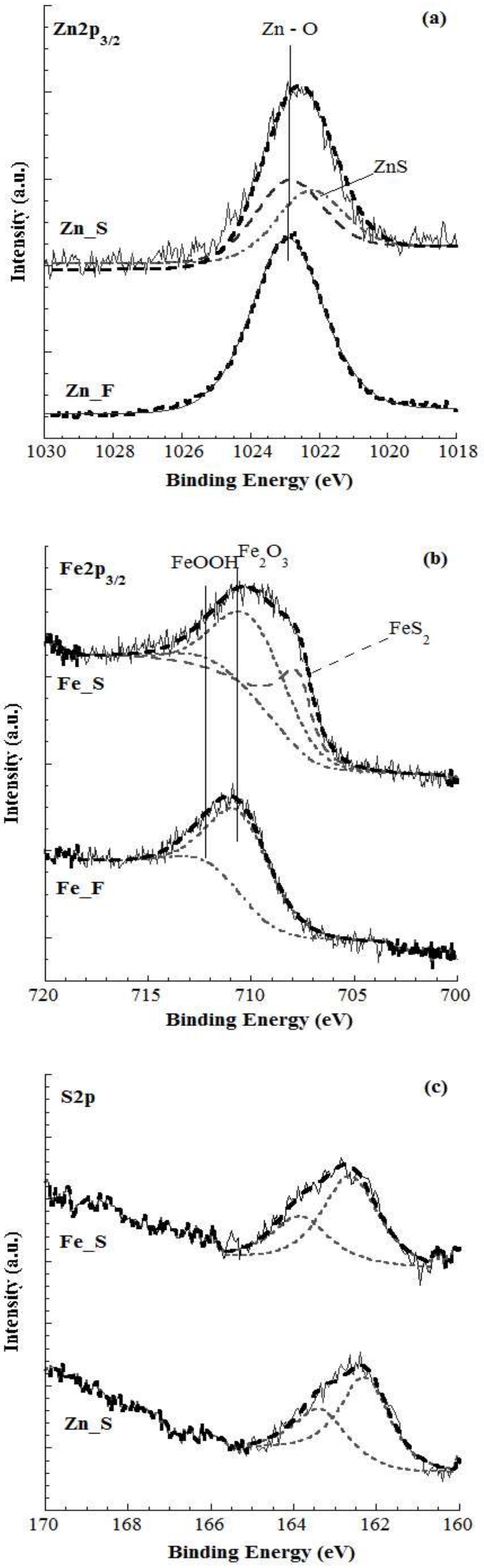
(a)
Zn2p3/2
Zn - O
ZnS
Zn_S
Zn_F
Intensity (a.u.)
1030
1028
1026
1024
1022
1020
1018
Binding Energy (eV)
(b)
Fe2p3/2
FeOOH
Fe2O3
FeS2
Fe_S
Fe_F
Intensity (a.u.)
720
715
710
705
700
Binding Energy (eV)
(c)
S2p
Fe_S
Zn_S
Intensity (a.u.)
170
168
166
164
162
160
Binding Energy (eV)

Figure 5

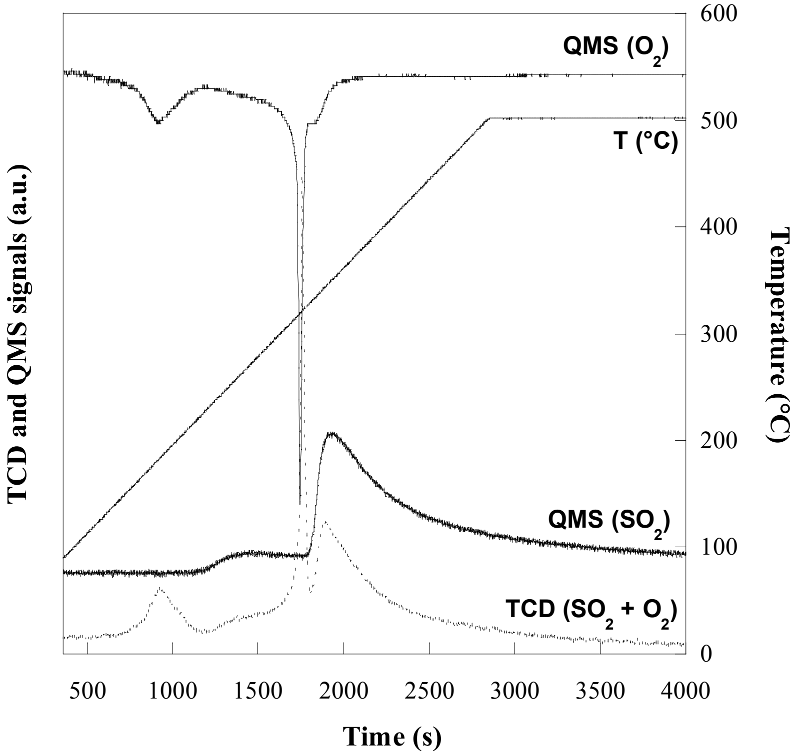

Figure 6

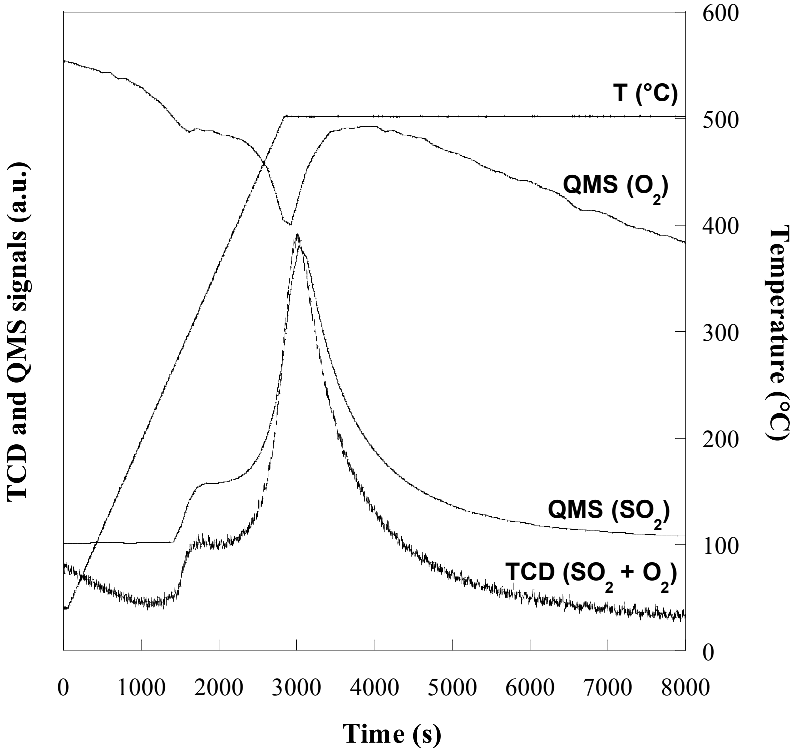

Figure 7

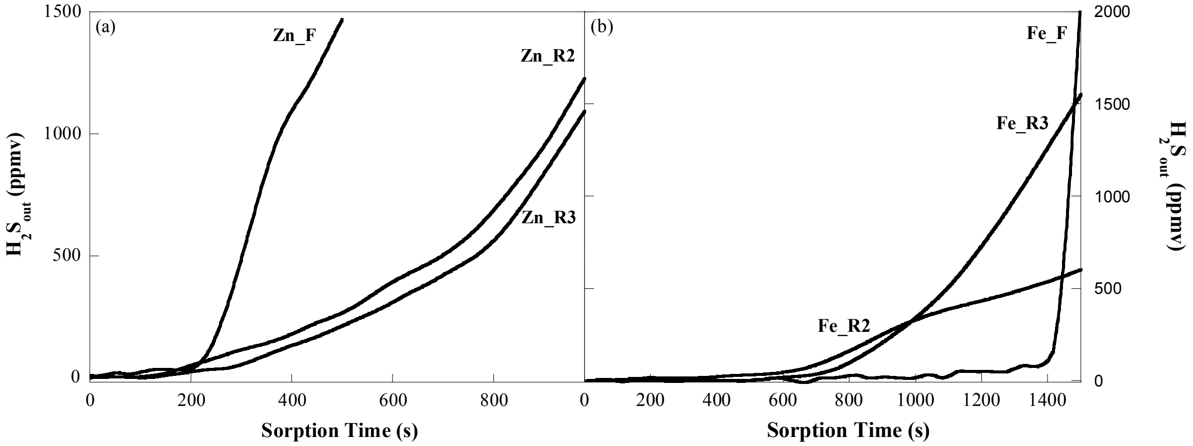
(a)
(b)
Zn_F
Zn_R2
Zn_R3
Fe_F
Fe_R3
Fe_R2
H_2S_{out} (ppmv)
1500
1000
500
0
200
400
600
800
Sorption Time (s)
2000
1500
1000
500
0
200
400
600
800
1000
1200
1400
Sorption Time (s)
H_2S_{out} (ppmv)

Figure 8

Table of contents entry

Novel MeO$_x$/SBA-15 (Me = Zn, Fe) nanosorbents exhibiting an excellent and durable performance for the H_2S removal from hot gas streams.